ETH
Eidgenössische Technische Hochschule Zürich
Swiss Federal Institute of Technology Zurich

IPA

On the feasibility of the low-ν method for SuperFGD

Till Dieminger

Semester project in the group of Prof. André Rubbia
Supervised by Dr. Christoph Alt & Dr. Davide Sgalaberna

August 14, 2021

ABSTRACT. The main goal of current and future long-baseline neutrino experiments is a precise measurement of the CP symmetry violating phase δ_{CP} in the leptonic sector. A major uncertainty in the determination of δ_{CP} in these experiments is due to a rather poor knowledge of the initial neutrino flux. Recently, a new flux measurement method has been established by the MINERνA experiment for neutrino energies from 2 - 50 GeV using the NuMI neutrino beam at Fermilab [1]. This so-called low-ν method sudies neutrino interactions with low hadronic recoil energies. For low-ν interactions, the neutrino cross-section is constant over a wide energy range, which enables a precise prediction of the flux shape. In this report, the feasibility of the low-ν method at the T2K experiment is studied with Monte Carlo simulations for the upgraded ND280 near detector. Neutrino interactions are simulated inside the new SuperFGD module and the outgoing particles are smeared according to the detector response. It is shown that, for the cut on the hadronic recoil energy ν that is required to reach a constant cross-section around the peak energy of the T2K neutrino flux of 0.6 GeV at the ND280 location, the number of expected neutrino interactions is too low to make a good prediction of the flux shape.

CONTENTS

List of Figures

Acknowledgments

I Introduction

In this section, the fundamentals of neutrino oscillations and CP violation are summarized. Further, the setup of the T2K experiment is explained briefly.

I.1 Neutrinos, the Standard Model and δ_{CP}

The standard model includes three flavors of massless WEYL leptons, called neutrinos. They are postulated to be left-handed, while their anti-particles are exclusively right-handed. Under these assumptions, the flavor of each neutrino is invariant under propagation.

The measurement of neutrinos coming from the Sun showed a deficit in muon neutrinos, hinting at a possible change of neutrino flavor under propagation. It was theorized that the mass eigenstates are a non-trivial superposition of the different flavors, also called the weak eigenstates. For this to be possible, the masses of at least two neutrinos have to be non-vanishing. One can use the so-called PONTECORVO-MAKI-NAKAGAWA-SAKATA matrix for the transformation between the mass and weak eigenstates:

$$
\begin{pmatrix} \nu_e \\ \nu_\mu \\ \nu_\tau \end{pmatrix} = \begin{pmatrix} U_{e1} & U_{e2} & U_{e3} \\ U_{\mu1} & U_{\mu2} & U_{\mu3} \\ U_{\tau1} & U_{\tau2} & U_{\tau3} \end{pmatrix} \begin{pmatrix} \nu_1 \\ \nu_2 \\ \nu_3 \end{pmatrix}
$$

$$
= \begin{pmatrix} 1 & 0 & 0 \\ 0 & \cos\theta_{23} & \sin\theta_{23} \\ 0 & -\sin\theta_{23} & \cos\theta_{23} \end{pmatrix} \begin{pmatrix} \cos\theta_{13} & 0 & \sin\theta_{13}e^{-i\delta_{CP}} \\ 0 & 1 & 0 \\ -\sin\theta_{13}e^{-i\delta_{CP}} & 0 & \cos\theta_{13} \end{pmatrix} \begin{pmatrix} \cos\theta_{12} & \sin\theta_{12} & 0 \\ -\sin\theta_{12} & \cos\theta_{12} & 0 \\ 0 & 0 & 1 \end{pmatrix} \begin{pmatrix} \nu_1 \\ \nu_2 \\ \nu_3 \end{pmatrix}. \tag{1}
$$

This matrix has four independent parameters $\theta_{12}, \theta_{23}, \theta_{13}$ and δ_{CP}. The three angles determine the extent of mixing and δ_{CP} is a possible complex phase, which would result in complex matrix elements.

Since the neutrinos interact in the weak eigenstates, while the propagation uses the mass eigenstates, an oscillation between different weak eigenstates can be observed. The probability to detect a neutrino in the weak eigenstate β that started in the weak eigenstate α is given as $\left\| \langle \nu_\beta | \nu_\alpha(t) \rangle \right\|^2$. For the propagation of $|\nu_\alpha\rangle$ the mass eigenstates $|\nu_i\rangle$ are used, as they evolve as $|\nu_i(t)\rangle = \exp(-iE_i t)|\nu_i\rangle$. At time t this expression is then rewritten in terms of the weak eigenstates $|\nu_\sigma\rangle$:

$$
|\nu_\alpha(t)\rangle = \sum_i U_{\alpha,i} \exp(-iE_i t)|\nu_i\rangle = \sum_{i,\sigma} U_{\alpha,i} e^{-ipt} \exp\left(-i\frac{m_i^2 t}{2E}\right) U_{\sigma,i}^\dagger |\nu_\sigma\rangle. \tag{2}
$$

The oscillation probability, i.e. the probability to measure ν_β at time t, is now given by :

$$
\mathscr{P}(\nu_\alpha \to \nu_\beta) = \left\| \langle \nu_\beta | \nu_\alpha(t) \rangle \right\|^2 \tag{3}
$$

$$
= \delta_{\alpha\beta} - 4\sum_{i>j} \Re(U_{\alpha i}^\dagger U_{\beta i} U_{\alpha j} U_{\beta j}^\dagger) \sin^2\left(\frac{\Delta m_{ij}^2 L}{4E}\right) + 2\sum_{i>j} \Im(U_{\alpha i}^\dagger U_{\beta i} U_{\alpha j} U_{\beta j}^\dagger) \sin\left(\frac{\Delta m_{ij}^2 L}{4E}\right),
$$

where L is the traveled length and $\Delta m_{ij}^2 = m_i^2 - m_j^2$. Doing the same calculation for $\mathscr{P}(\overline{\nu}_\alpha \to \overline{\nu}_\beta)$, the sign in front of the imaginary part flips. Assuming CP-symmetry to hold, those two probabilities should be identical. The term possibly violating the CP-symmetry is therefore connected to the complex part of the PMNS matrix. A trivial phase would mean that CP-symmetry holds, while any non-trivial phase would result in the breaking of this symmetry.

A possible CP-asymmetry is especially interesting since it could offer a possible explanation for the matter-antimatter asymmetry in the universe. The violation in the leptonic sector can be translated into a Baryon asymmetry within the framework of leptogenesis. The breaking of CP-symmetry in the leptonic sector is

required since the violation in the hadronic sector is not strong enough to explain the currently observed asymmetry of matter and anti-matter.

If neutrinos propagate through matter, the neutral and charged current interactions have to be taken into account for the oscillation probability. The neutral current interactions affect all three flavors in the same manner, while the charged current only plays a significant role for the electron-neutrinos, since the matter of earth only contains electrons and no muons or taus. This leads to a changed propagation law, which can be phenomenologically described as

$$i\partial_t |\nu_\alpha(t)\rangle = (\mathcal{H}_{vac} + V) |\nu_\alpha(t)\rangle, \qquad V = \begin{pmatrix} \sqrt{2}G_F n_e & 0 & 0 \\ 0 & 0 & 0 \\ 0 & 0 & 0 \end{pmatrix}. \tag{4}$$

Taking into account these matter effects and expanding the PMNS matrix for $\mu \to e$ the oscillation probability is given as [2]:

$$\begin{aligned}
\mathcal{P}(\nu_\mu \to \nu_e) =& 4c_{13}^2 s_{13}^2 s_{23}^2 \cdot \sin^2\Phi_{31} \\
&+ 8c_{13}^2 s_{12} s_{13} s_{23} (c_{12} c_{23} \cos\delta_{CP} - s_{12} s_{13} s_{23}) \cdot \cos\Phi_{32} \sin\Phi_{31} \sin\Phi_{21} \\
&- 8c_{13}^2 c_{12} c_{23} s_{12} s_{13} s_{23} \sin\delta_{CP} \sin\Phi_{32} \sin\Phi_{31} \sin\Phi_{21} \\
&+ 4s_{12}^2 c_{13}^2 (c_{12}^2 c_{23}^2 + s_{12}^2 s_{23}^2 s_{13}^2 - 2c_{12} c_{23} s_{12} s_{13} \cos\delta_{CP}) \cdot \sin^2\Phi_{21} \\
&- 8c_{13}^2 c_{13}^2 s_{23}^2 \frac{aL}{4E_\nu} (1 - 2s_{13}^2) \cdot \cos\Phi_{32} \sin\Phi_{31} \\
&+ 8c_{13}^2 s_{13}^2 s_{23}^2 \frac{a}{\Delta m_{31}^2} (1 - 2s_{13}^2) \cdot \sin^2\Phi_{31}.
\end{aligned} \tag{5}$$

Here c_{ij} and s_{ij} are short for $\cos\theta_{ij}$ and $\sin\theta_{ij}$ respectively and Φ_{ij} was used for $\Delta m_{ij}^2 L/4E$. The matter effects are summarized in the parameter a. The first term of equation 5 is the quasi-two-neutrino oscillation probability, the second term is CP invariant and the third term possibly violates CP symmetry. The fourth term is the so-called solar term and the last two terms are the included matter effects. To understand why the second and third terms are CP invariant and violating respectively, one has to calculate the same probability after a CP transformation; meaning $\mathcal{P}(\overline{\nu}_\mu \to \overline{\nu}_e)$. This results in the same equation but changing $\delta \mapsto -\delta$) in all terms. While the second term is symmetric under this transformation, the third one is not, meaning that it violates the CP-symmetry if δ_{CP} is non-zero. This effect can be seen in fig. 1, where the individual contributions to the corresponding oscillation probability are shown. One can see that the blue dotted line, corresponding to the third term, is different for the neutrino and anti-neutrino oscillation. This is the effect of the CP violation in the leptonic sector. Further, the effects of matter are not the same for neutrinos and anti-neutrinos. This can be analyzed and used to determine the sign of Δm^2.

A precise measurement of the oscillation probabilities $\mathcal{P}(\nu_\mu \to \nu_e)$, $\mathcal{P}(\overline{\nu}_\mu \to \overline{\nu}_e)$ and knowledge of the three mixing angles determines δ_{CP} and with this, allows measurement of possible CP-violations in the leptonic sector.
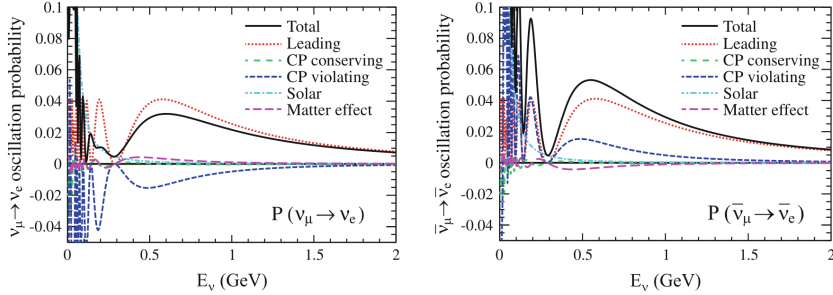
Figure 1: Determination of δ_{CP} using the oscillation probability, taken from [2]. The CP-violating term has a different sign for neutrino and anti-neutrino interactions. This can be used for a determination of δ_{CP}. The matter effect introduces additional differences between neutrinos and anti-neutrinos.

I.2 δ_{CP} and the T2K Experiment

T2K is a long-baseline neutrino-oscillation experiment in Japan that uses the J-PARC beam facilities. At J-PARC, a proton beam impinging on a target generates secondary hadrons. Most of these hadrons are pions, which predominately decay into a muon and a muon-neutrino to produce the neutrino beam. Using a focusing horn, one can select positive or negative hadrons, leading to a $\bar{\nu}$ or ν beam. Contamination of the muon-neutrino beam with electron-neutrinos comes from the muon decaying to an electron, a muon-neutrino, and an electron-neutrino. A small fraction of pions decay into an electron and electron-neutrino, which leads to further contamination of the beam.
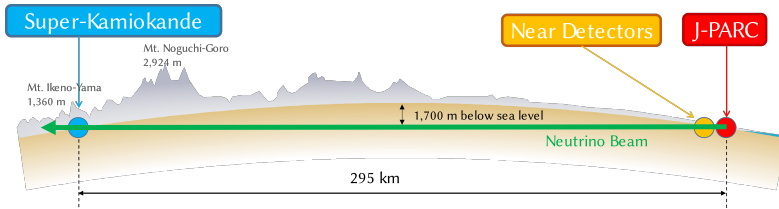

Figure 2: Schematic of the T2K experiment in Japan. Taken from the T2K collaboration.

At a distance of 280m from the decay point, the three near detectors are installed. These detectors are INGRID, WAGASCI-Baby MIND, and ND280. INGRID is an on-axis detector, WAGASACI is 1.5 degrees off-axis and ND280 is 2.5 degrees off-axis. The far detector Super Kamiokande is located 295 km away and 2.5 degrees off-axis. Using the off-axis configuration results in a narrower neutrino flux peak at lower energies compared to the neutrino flux on axis. For the beam to peak at a neutrino energy of E_ν, the off-axis angle has to be chosen in a way such that:

$$E_\nu = \frac{m_\pi^2 - m_\mu^2}{2(E_\pi - p_\mu \cos\theta_\nu)}. \tag{6}$$

Here θ_ν is the angle between the pion direction and the neutrino in the lab frame. Since the pions are strongly boosted along the beam direction, this angle is approximately equal to the off-axis angle. E_ν is the neutrino energy coming from the π decay and p_X, m_X are the absolute value of the momentum and the mass of particle X respectively.

This work focuses on the ND280 detector, more specifically the upgrade including the so-called Super Fine Graded Detector (SuperFGD).

The neutrino energy spectrum after oscillation is:

$$N(E_v) = \int \Phi(E_v, t) \times \sigma(E_v) \times R_{detector}(E_v, \sigma, \vec{p}) \times P_{osc}(E_v). \tag{7}$$

Here $N(E_v)$ is the measured neutrino energy spectrum at the far detector, Φ is the flux before oscillation, σ is the neutrino cross-section, R is a collection of the detector responses, and P_{osc} is the oscillation probability. As can be seen from equation 7, the initial neutrino flux is an important input parameter for the oscillation measurements, but predictions of the flux from hadron interaction models have large uncertainties. Therefore, the main purpose of the ND280 detector is to measure the initial flux as well as neutrino cross-sections.

Before the recent upgrade, the upstream half of ND280 was a π^0 detector that discriminates the $\pi^0 \rightarrow \gamma\gamma$ background, which could mimic a v_e charged current interaction. This part was partially replaced with the SuperFGD, which is introduced below. Downstream of the π^0 detector, three time projection chambers together with two fine-grained detectors measure the charged current interactions. Choosing the beam direction as the z axis, the FGDs are made from scintillator bars aligned in either the x or y direction. This setup is surrounded by an electromagnetic calorimeter and the refurbished UA1 magnet, providing a magnetic field of 0.2 Tesla.

The SuperFGD, which replaces the majority of the π^0 detector, is built out of roughly 2 million polystyrene-based scintillator cubes doped with 1.5% paraterphenyl (PTP) and 0.01% of POPOP. Each cube has a size of $1 \times 1 \times 1 cm^3$. Due to a surface treatment, they are optically independent and can be read out by three orthogonal wavelength shifting fibers. This cube design enables the detector to detect very short tracks of charged particles with good spatial resolution, as they are generated in e.g. neutron interactions. It also enables high efficiency for the full solid angle while maintaining the high active mass (approximately 2 tons) necessary in neutrino experiments. The wavelength shifting fibers are read out at the side of the SuperFGD by Multi-Pixel-Photon Counters. The SuperFGD is sandwiched in between two time projection chambers for muon identification. In front of this stack of detectors, a thin π^0 detector is installed, acting as a veto for non-decayed pions.

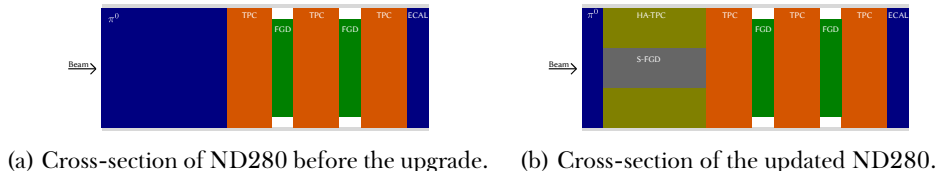(a) Cross-section of ND280 before the upgrade.   (b) Cross-section of the updated ND280.

Figure 3: Schematic of the ND280 detector of T2K.

II   Theory

In this section, the basics of neutrino interactions and detection are discussed. Different methods to distinguish events on hydrogen from those on carbon are summarized and the principle of the low-ν method is explained.

II.1   Neutrino Detection

Neutrino interactions can be separated into two main categories. The first one is the so-called neutral current interaction, which is an exchange of a Z^0 boson with another particle. In this case, the leptonic part of the initial and final state are identical, since the neutrino will be part of the in- and out-going state. These interactions are therefore flavor insensitive. The second kind of interaction is the charged current interaction (CC), where a neutrino interacts with another particle under the exchange of a W boson. The initial state neutrino enters the final state as a lepton of the same flavor as the neutrino. The initial neutrino-flavor is then taggable by the outgoing lepton. The charge of the outgoing lepton determines if the initial state included a neutrino or anti-neutrino. This enables a good estimation of the initial composition of the beam.

A neutrino can interact with single electrons, whole nuclei, single or correlated nucleons, and single quarks. At the energies of the T2K flux, the predominant interaction mode is quasi-elastic scattering (QE), in which the neutrino scatters off a single nucleon, which stays intact after the interaction. This is appealing for oscillation experiments since the charged leptons tag the incoming neutrino and a simple reconstruction of the neutrino energy from the kinematics of the lepton is possible. Using the conservation of four-momentum, the energy of the anti-neutrino E_ν is calculated to be:

$$E_\nu^{CCQE} = \frac{m_N^2 - m_P^2 - m_\mu^2 + 2m_P E_\mu}{2(m_P - E_\mu + p_\mu \cos(\theta_\mu))}.$$

(8)

Here m_X is the mass of the neutron, proton, or muon, and p_μ is the absolute value of the muon-momentum. The angle θ_μ is the angle between the incoming neutrino and the outgoing muon. This reconstruction is correct for the scattering on free nucleons as in hydrogen targets, but only approximate for other atoms. Nucleons in a larger core interact with each other and are not at rest with respect to the lab frame but have a relative momentum, called Fermi-motion. This Fermi-motion leads to a smearing of the reconstructed
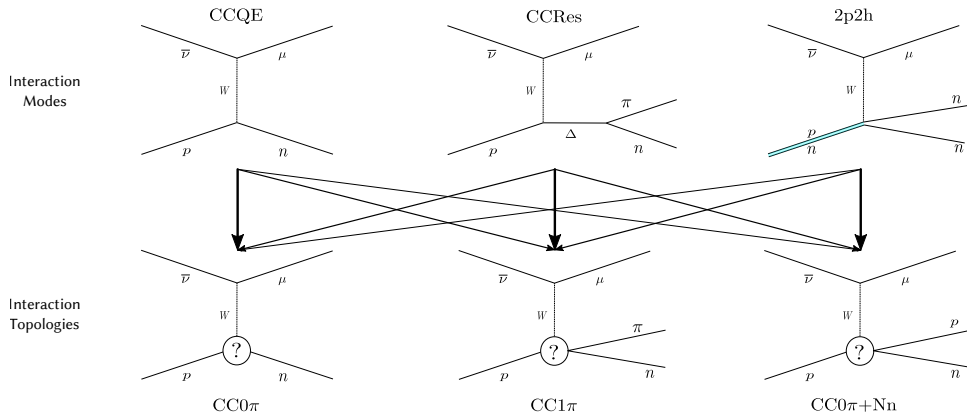
Figure 4: The charged current topologies and modes. The modes are different physical processes while the topologies are what is seen in the detector. Each topology has a contribution from all the modes due to final state interactions. Adapted from reference [3].

energy when a neutrino interacts with a larger nucleus, e.g. carbon. The Fermi-motion and binding energies of nucleons are modeled using so-called spectral functions, e.g. the so-called effective spectral function. The

charged current quasi-elastic (CCQE) scattering of anti-neutrinos is detected as an event where a neutron is ejected from the nucleus and a muon is emitted (compare fig. 4). This is called the CC0π topology since no final state pions are visible.

In general, the physical process is called interaction mode, while the final state of a given process can include further particles that come from possible secondary interactions. This final state, which is then detected, is called topology. The topology for a charged lepton and pion in the final state is called CC1π. This can happen when the struck nucleon gets excited into resonance and then decays back to the ground state, emitting a pion. The name of this mode is CCRes or resonance mode. But the CC1π topology could also originate from a CCQE mode, where the stuck neutron interacts inside a larger nucleus, like carbon, with other nucleons. In such an event, a pion is produced in the neutron-nucleon scatter, resulting in a CC1π topology where the energy of the neutron is reduced. Another possibility is that the nucleon could lose some energy, without producing a pion, before leaving the nucleus, resulting in a CC0π topology with the neutron having reduced its energy as well. A CCRes event could also end up in the CC0π topology if the pion gets absorbed inside the nucleus. For heavy nuclei, it is therefore not possible to determine which interaction mode generated a specific topology on an event-by-event basis and one needs to rely on nuclear models with large uncertainties for statistical analyses. Neutrinos scattering off correlated pairs of nucleons in so-called 2p2h interactions can also produce CC0π topologies, further complicating the issue. However, the majority of CCQE interactions will appear as CC0π topologies inside the detector.

Even assuming a perfect detector, these effects lead to a smearing of the energy reconstruction using equation 8. Since the interactions of absorbing or emitting a pion are not present in hydrogen, the CC0π events on hydrogen will come purely from CCQE interactions and vice versa, assuming that the detector can reconstruct every present pion. Since the contributions to CC0π topologies from non-CCQE interactions become larger in large nuclei, a detector with a large fraction of hydrogen is very appealing for the reconstruction of neutrino energies and thus flux measurements.

II.2 Low ν Method

Experiments can measure the neutrino interaction rate as a function of neutrino energy. The interaction rate is the product of the incoming neutrino flux and the neutrino cross-section. Cross-sections for scattering on nuclei are not precisely known and their uncertainties often dominate the flux measurements. Therefore an energy-independent, 'flat' cross-section can be used to measure the shape of the flux, which would be identical to the shape of the interaction rate. However, this method still leaves the overall normalization of the flux unknown.

A calculation of the cross-section with respect to the recoil energy $\nu = \frac{p_{\mathcal{N}} \cdot q_W}{M_{\mathcal{N}}} = E_\ell - E_\nu$ is given in the appendix and results in:

$$\frac{d\sigma}{d\nu} = \frac{G_F^2 M_{\mathcal{N}}}{\pi} \int_0^1 \left(F_2 - \frac{\nu}{E_\nu} [F_2 \mp x F_3] + \frac{\nu}{2E_\nu^2} \left[\frac{M_{\mathcal{N}} x(1-R_L)}{1+R_L} F_2 \right] + \frac{\nu^2}{2E_\nu^2} \left[\frac{F_2}{1+R_L} \mp x F_3 \right] \right) dx. \qquad (9)$$

Here G_F is the Fermi constant, $M_{\mathcal{N}}$ is the mass of the struck nucleon, F_i are the structure functions, $R_L = \frac{F_2}{2xF_1}$ and the '+' corresponds to the neutrino, while '-' to the anti-neutrino. In the case where $\nu \ll E_\nu$, the cross-section becomes independent of E_ν since all the energy-dependent terms become negligible. The cross-section therefore is simply given as:

$$\frac{d\sigma}{d\nu} \rightarrow \frac{G_F^2 M_{\mathcal{N}}}{\pi} \int_0^1 F_2 \, dx. \qquad (10)$$

Here F_2 is a structure function, which is approximately energy independent. One can thus determine the shape of the flux by selecting events with low-ν.

Due to the finite value of ν in real experimental setups and the Bjorken scaling violation of the structure constants, the experimental low-ν cross-section in equation 10 is not perfectly constant, which introduces a systematic uncertainty.

III Analysis

In this section a generated Monte Carlo set of neutrino events is analyzed for the feasibility of the low-ν method. This is done in several steps. In sections III.1 through III.4, the true Monte Carlo values are analyzed and the resulting cross-sections are shown for different cuts on ν in order to evaluate the feasibility of the low-ν method for a perfect detector and to highlight the intrinsic challenges of this method for T2K. Subsequently, the detector effects are included and the final results are presented by using a toy Monte Carlo to determine the statistical uncertainties.

III.1 Data Sample & Event Selection

A NEUT Monte Carlo simulation of $1\,000\,000$ anti-muon-neutrino events, generated with the T2K flux at 2.5 degrees off-axis, is used, see fig. 5. NEUT is a program library to simulate neutrino interactions with nuclei [4]. The Monte Carlo sample is equivalent to an exposure of approximately 43×10^{21} PoT·ton. For the neutrino interaction, the Monte Carlo simulation assumed a target consisting of hydrogen and carbon with a fraction of 1:1, as it is the case for SuperFGD. For the nuclear model, the effective spectral function was used together with a quasi-elastic vector mass $M_A = 1.03$ GeV.

Since the inclusion of detector effects was restricted to events with neutrons of an energy below 800 MeV, all events with neutrons above this threshold are not considered. This affects roughly 0.3% of total events. To evaluate the statistical uncertainties of the detector effects, a Toy Monte Carlo was used.

Since T2K mainly records CCQE like events, the interaction topology CC0π with no final state pions was chosen. For $\overline{\nu}_\mu$-CCQE interactions ($\overline{\nu}_\mu + p \rightarrow \mu^+ + n$) at least one neutron is expected in the final state. Therefore the selection criteria require at least one final state neutron.

If any final state proton is present, it is required to have kinetic energy below 10 MeV. This is done to include possible events where the detector missed a low energy proton. Above 10 MeV the proton detection efficiency of SuperFGD is assumed to be high enough for those events to be vetoed.

To summarize, the event selection rules are as follows:

- At least one neutron in the final state and no final state pions (CCQE)

- No final state protons or only protons below 10 MeV kinetic energy (CCQE)

- Neutron below 800 MeV kinetic energy (limited by the range of detector smearing matrices).

These selection criteria are fulfilled by $371\,552$ events. The data set includes $406\,518$ real CCQE events and the purity in selecting CCQE events is given by $^{(\text{Selected \& CCQE})}/_{\text{Selected}} = 0.90386$. A more restrictive cut on the proton momentum of 1 MeV increases the purity only slightly to 0.9047. For each event, NEUT provided the information if the neutrino scattered on a hydrogen or carbon nucleus. This information is used in the following sections and plots.
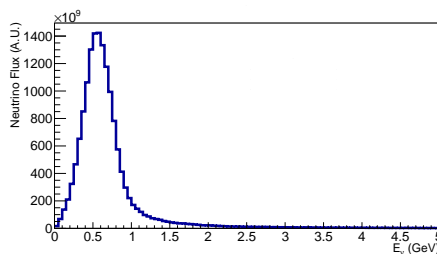

Figure 5: The T2K flux at 2.5 degrees off-axis used in the simulation. The peak energy is around 600 MeV which maximizes the oscillation probability at the T2K far detector distance of 295 km.
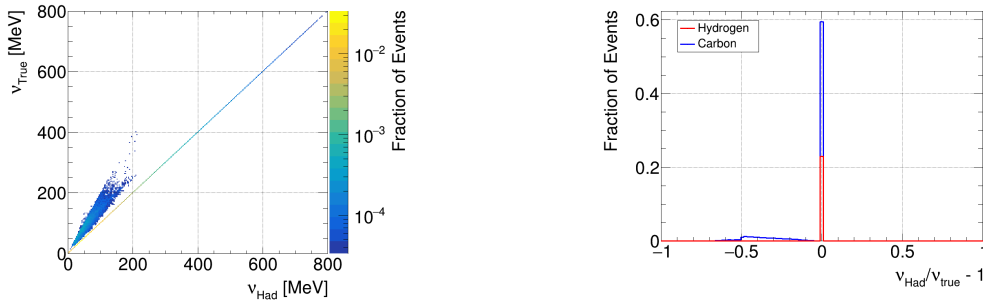
III.2 Recoil Energy

The variable ν_{true} is the recoil energy returned by the NEUT generator and will be assumed to be the true recoil energy. It is the kinetic energy of the nucleus directly after the interaction, where no final state interactions are taken into account, while the potential Fermi motion is. For the reconstruction, the recoil energy ν of the nucleon was defined by the kinetic energy of the final state neutron as:

$$\nu_{Had} = E_N^{kin}. \tag{11}$$

This is called the hadronic reconstruction. If several neutrons are present in the final state, the one with the highest momentum is considered as the one connected to the interaction.

Another option would be the leptonic reconstruction using $\nu_{\text{Lep}} = E_\nu^{\text{CCQE}} - E_\mu + \Delta M$. When comparing those two methods in fig. 6 and fig. 7 it can be seen that the hadronic reconstruction is less widespread and has a higher fraction of well-reconstructed events.

(a) Distribution of the hadronic recoil energy against the true recoil from NEUT. The diagonal shows a high fraction of perfectly reconstructed recoil energies. The other events have their recoil energy underestimated.

(b) Resolution of the hadronic recoil energy. A high fraction of recoil energies is perfectly reconstructed. In the underestimated energies the cutoff at -0.5 is possibly due to generator implementations.

Figure 6: Hadronic reconstruction.
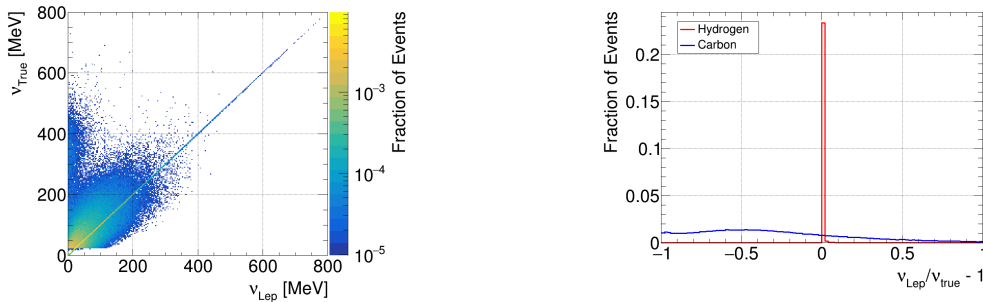
(a) Distribution of the leptonic recoil energy against the true recoil from NEUT. The diagonal shows the perfectly reconstructed recoil energies. The other events are smeared around this diagonal.

(b) Resolution of the leptonic recoil energy. A high fraction of recoil energies is perfectly reconstructed. The events on carbon are wide spread with a heavier tail to the left.

Figure 7: Leptonic reconstruction.

A feature seen in both cases is the diagonal line of perfect reconstruction that comes from neutrino interactions on hydrogen, for which there are no final state interactions. For these events, both the hadronic and

leptonic reconstructions of ν are exact. But many interactions with carbon also do not undergo final state interactions and are therefore only affected by Fermi motion. These events are also well reconstructed using the hadronic method.

Focusing on the leptonic reconstruction in fig. 7b, a strong tail to the left can be seen. This corresponds to an underestimation of ν_{true} by ν_{Lep}. The reason for this is the CCQE-hypothesis (eq. 8) used for the reconstruction, which, on average, shifts the energy towards lower values with respect to E_ν^{true}, as can be seen in fig. 9 in the next section. This leads to an underestimation of the recoil energy.

Now looking at the reconstruction using the neutron in fig. 6b, a strong central peak, this time coming from both hydrogen and carbon can be seen. This is due to the fact, that both E_{kin}^N and ν_{true} include the Fermi-motion. If the neutron from scattering on carbon does not undergo final state interactions, it is therefore reconstructed to the same recoil energy as ν_{true}. This was not the case for the reconstruction using ν_{Lep}, since there the muon energy gets calculated using the CCQE-hypothesis, which assumes a resting nucleon. This central peak can then be used to estimate the fraction of neutrons from interactions on carbon which undergo final state interactions to be around 20%. The non-central contribution of the resolution is strictly to the left of the peak, meaning $\nu_{\text{Had}} \leq \nu_{\text{true}}$. This is due to the fact that, in NEUT, neutrons always lose energy in final state interactions. The cutoff at -0.5 means that the energy loss of neutrons in final state interactions is limited to half their kinetic energy. If the neutron loses energy, it is more probable to lose a higher fraction of its energy than a smaller fraction. This could be an effect of the used spectral functions, but more time would be needed to investigate this properly. In summary, the reconstruction using ν_{Had} is preferred over the reconstruction using ν_{Lep} and is used in the following analysis.

The hadronic recoil energy distribution in fig. 8a for hydrogen starts at zero, while for events on carbon, it starts at around 25 MeV. Comparing this to the true recoil energy distribution in fig. 8b, it can be seen that this is not a reconstruction artifact, but due to Pauli blocking in the composite nucleus of carbon. The presence of a nucleon with specific energy takes a certain region of the phase space, which is not available for the neutron resulting from the neutrino interaction. The nucleons in the nucleus sit below the Fermi energy, meaning that the struck nucleon has to have a momentum above this to find space in the phase space. Therefore this effect is dependent on the specific implementation of the spectral function in the generator. This effect is not present in hydrogen due to the lack of a composite nucleus. This results in a selection of mainly hydrogen events for strong ν cuts.

Figure 8c shows the mean recoil energy returned from the generator with respect to the energy of the incoming neutrino. A higher neutrino energy leads to higher recoil energies. Knowing that the mean of the flux is around 600 MeV, this shows that the majority of recoil energies is below 150 MeV.
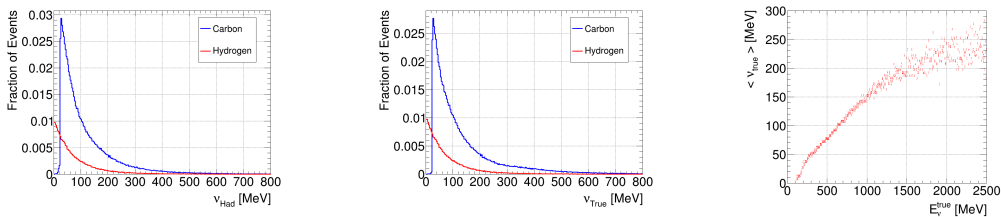
(a) Distribution of the hadronic recoil energy. See the cutoff at around 25 MeV due to Pauli blocking in carbon (blue).

(b) Distribution of the true recoil energy. See the cutoff at around 25 MeV due to Pauli blocking in carbon (blue).

(c) Mean of the recoil energy with respect to the incoming neutrino energy.

Figure 8: Distribution of the hadronic and true recoil energy

III.3 Neutrino Energy Spectra

The neutrino energy reconstruction was done using the CCQE hypothesis in equation 8. In the following figures of the energy distribution (fig. 9) and resolution (fig. 10), the ν-cuts of $10, 50, 100$ and 150 MeV are used in the corresponding subplots. The events on hydrogen are depicted in red, the ones on carbon in blue, and the combined events are shown in green. The corresponding reconstructed energy is shown as a solid line, while the true energy is depicted as a dotted line.

As mentioned above, the hardest cut $\nu < 10$ MeV includes mainly hydrogen events. This changes as soon as the cut is loosened to above 25 Mev.

Over the whole range of cuts, hydrogen events are reconstructed perfectly, which can be seen in the overlap of the solid and dotted red lines in fig. 9 and by the peak in the energy resolution plots in fig. 10. For carbon the reconstructed energy peak is shifted to lower values, meaning the CCQE hypothesis usually underestimates the neutrino energy.

A looser cut leads to a worse overall energy reconstruction. This can be seen by the larger area between the dotted and solid lines and the wider distribution in the resolution plots of the carbon component. In the later part of this work, the true energy of the neutrinos is used to calculate the cross-sections. This is done since the low-ν method is expected to be very challenging for measuring the flux at T2K energies, and a perfect neutrino energy reconstruction was assumed to validate the feasibility of this method under the best conditions by using the true neutrino energy.

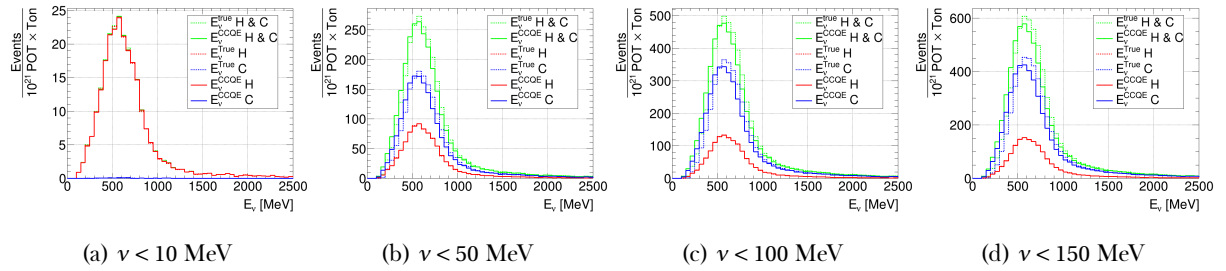| (a) $\nu < 10$ MeV | (b) $\nu < 50$ MeV | (c) $\nu < 100$ MeV | (d) $\nu < 150$ MeV |

Figure 9: Distribution of the reconstructed and initial neutrino energy. The true energy is depicted in dotted lines while the reconstructed one is shown as solid lines. For weaker cuts, the CCQE hypothesis underestimates the true recoil energy. The weaker the cuts, the stronger this effect.
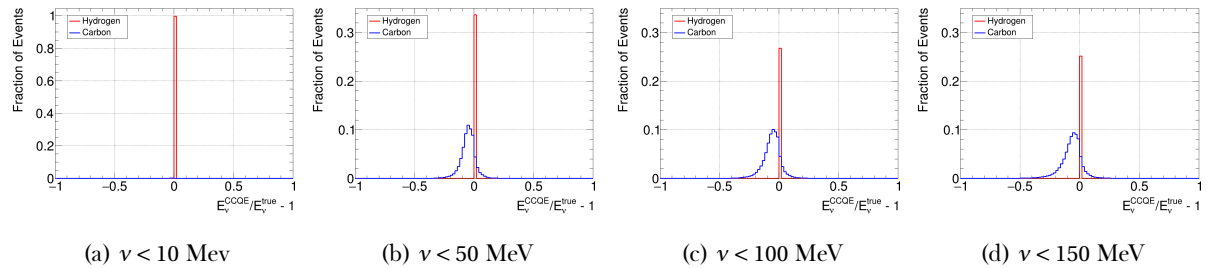
| (a) $\nu < 10$ Mev | (b) $\nu < 50$ MeV | (c) $\nu < 100$ MeV | (d) $\nu < 150$ MeV |

Figure 10: Resolution of the energy reconstruction for different cuts on ν. In all figures a perfect reconstruction on hydrogen can be seen. For carbon the reconstructed energy is smaller than the true energy.

III.4 Cross-Section

The cross-section in the chosen selection is calculated by dividing the number of events in each energy bin, after event selection and cut on ν, by the corresponding neutrino flux given by NEUT. This then has to be corrected by an overall scale factor to get the cross-section in units of nb/nucleon.

In the following figures 11a, 11b, and 12, the cross-sections for different ν-cuts are shown for events on hydrogen and carbon individually and combined. A hard cut on $\nu < 10$ MeV results in a constant cross-section over the whole considered energy range. The weaker the cut, the more the cross-section deviates from a constant value. This is expected given the dependence of the cross-section on ν as derived in equation 10. Looking at the different contributions from hydrogen and carbon, it becomes apparent that the cross-section gets constant at lower energies for hydrogen than it does for carbon. This is true for all the ν-cuts. For carbon, no events survive the cut of $\nu < 10$MeV, due to the Pauli blocking discussed earlier. It can be seen from these plots that the low-ν method is very challenging, even when using the true Monte Carlo values without detector smearing, as a constant cross-section at the T2K neutrino beam energy peak of around 600 MeV can only be achieved with very hard cuts on ν of about 10 MeV.
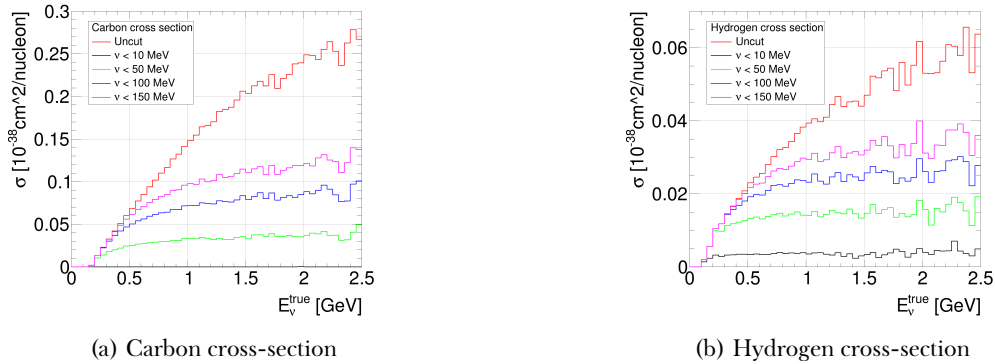

(a) Carbon cross-section

(b) Hydrogen cross-section

Figure 11: Cross section for hydrogen and carbon. The different colors correspond to different cut offs in ν. For carbon the $\nu < 10$ MeV cross-section is not visible due to the effects of Pauli blocking.
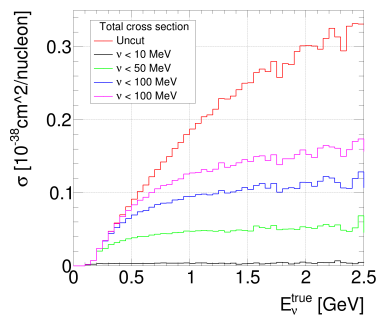

Figure 12: Cross-section for carbon and hydrogen combined with different cuts on ν.

III.5   Detector Smearing

The analysis above was done without considering any detector effects. Those effects are integrated into the analysis in this section. Since the calculation of the cross-section uses the true and not the reconstructed neutrino energy, the detection of the muon is not necessary to estimate the neutrino energy. Therefore the detector effects on the muon are not considered and only the effect on the neutron will be included. The smearing of the neutron will affect the number of events passing a certain cut on ν and therefore affect the corresponding cross-section.

III.5.*i*   Detection & Smearing

The SuperFGD is built from $1 \times 1 \times 1 cm^3$ scintillator cubes stacked together. This is schematically depicted in fig. 13. If an anti-neutrino enters the detector and interacts, it will leave an energy deposit in the corresponding cube, which will be identified as the initial reaction point at time t_1. An anti-muon will travel through the detector leaving a trail of small energy deposits in the scintillators. The neutron on the other hand will propagate a certain apparent length ℓ, possibly scattering on other nuclei without depositing visible amounts of energy. At time t_2, an interaction of the neutron will deposit a detectable amount of energy in one of the cubes. Using the time of flight information and the neutrons apparent travel distance, the so-called lever arm ℓ, the kinetic energy of the neutron can be calculated:

$$E_{kin} = m \left(\frac{1}{\sqrt{1 - \beta^2}} - 1 \right), \quad \beta = \frac{\ell}{\Delta t}. \tag{12}$$

Since the spatial resolution on the traveled length is $1 cm$, the detection of neutrons with a relatively short lever arm has a bigger relative uncertainty on the kinetic energy, leading to a wider spread. Because of this, the detector simulation includes 7 smearing matrices in intervals of 10 cm for lever arms up to 70 cm. The last matrix extends up to a lever arm of 100 cm. These smearing matrices were generated by a GEANT4 simulation of neutrons in SuperFGD with a time resolution of $\max\left(0.95 \times \sqrt{40 PE/3LY}\, ns, 200 ps\right)$. Here PE is the number of photoelectrons and LY is the light yield of the neutron cluster. The $\sqrt{3}$ in the denominator is due to the three readout fibers and the lower limit due to the readout electronics. The smearing matrix for lever arms between 10 and 20 cm is shown in fig. 14. Having determined the lever arm of an event, the corresponding smearing matrix is chosen. The generated kinetic energy is taken from the simulation and the corresponding bin in the smearing matrix is selected, leading to a one-dimensional random distribution of the kinetic energy. This distribution is then randomly sampled to return the smeared kinetic energy for this event.

Due to possible invisible scatterings on the track of the neutron, the traveled length of some neutrons is underestimated, which leads to a systematic shift to lower kinetic energies.
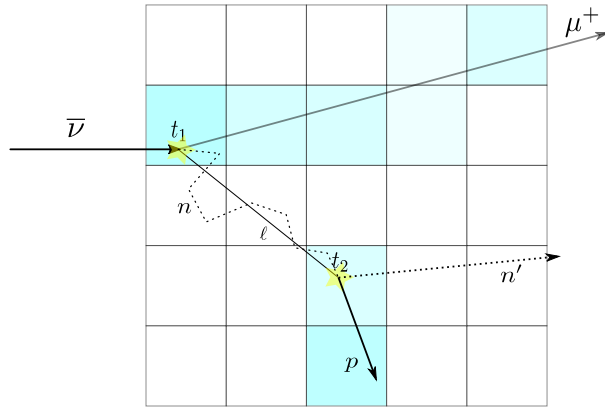
Figure 13: Detection of an $\overline{\nu}$ event in SuperFGD. The neutrino interacts with a proton, emitting a muon at t_1. The resulting neutron scatters invisibly until it gets detected at t_2. The lever arm is estimated as ℓ. The kinetic energy is reconstructed using the time of flight and the lever arm. Adapted from reference [5]
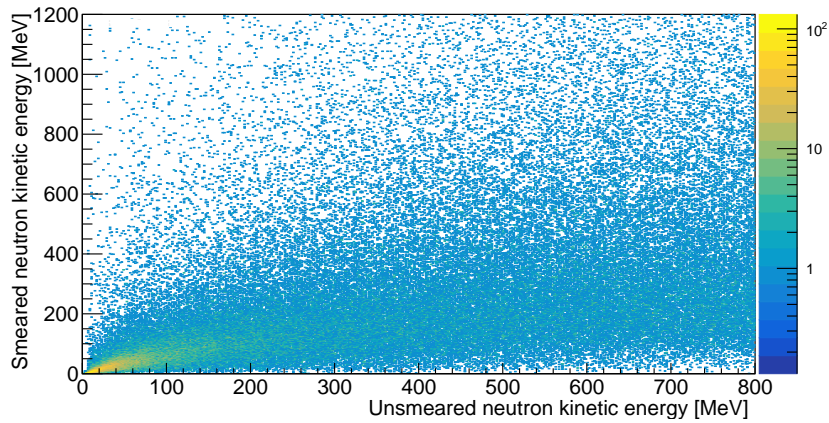

Figure 14: Example smearing matrix for a lever arm of 10 to 20 cm. On the x-axis the unsmeared neutron kinetic energy and on the y-axis the smeared neutron kinetic energy is shown. For a certain value of the unsmeared kinetic energy, a random sampling of the corresponding 1D-histogram is taken to determine the smeared kinetic energy.

III.5.ii Effects

The detector effects of SuperFGD can be seen in fig. 15. Events on hydrogen and carbon get affected in different ways. The smearing for the events on carbon is wider than for the events on hydrogen and shifted to lower values ($\nu_{\text{smeared}} < \nu_{\text{unsmeared}}$). This can be understood by recalling that the neutrons coming from events on carbon, on average, have higher energy compared to events on hydrogen, which can be seen in fig. 8, where the distribution of the neutron kinetic energy, which by definition is equal to the recoil energy ν, is depicted. The limited time resolution of the detector leads to larger relative smearing for fast neutrons, which in turn leads to a worse resolution for events on carbon.

Possible neutron interactions inside the detector are elastic and inelastic scattering on carbon and elastic scattering on hydrogen. The elastic scattering on carbon can change the direction of neutrons without depositing a visible amount of energy, leading to an underestimation of the traveled path, and therefore also to an underestimation of the recoil energy. The relative cross-section for elastic neutron scatters on carbon is highest around the peak energy of neutrons coming from neutrino interactions on carbon, which explains why these neutrons are slightly shifted to lower energies in the smearing process.

(a) $\nu < 10$ MeV

(b) $\nu < 50$ MeV

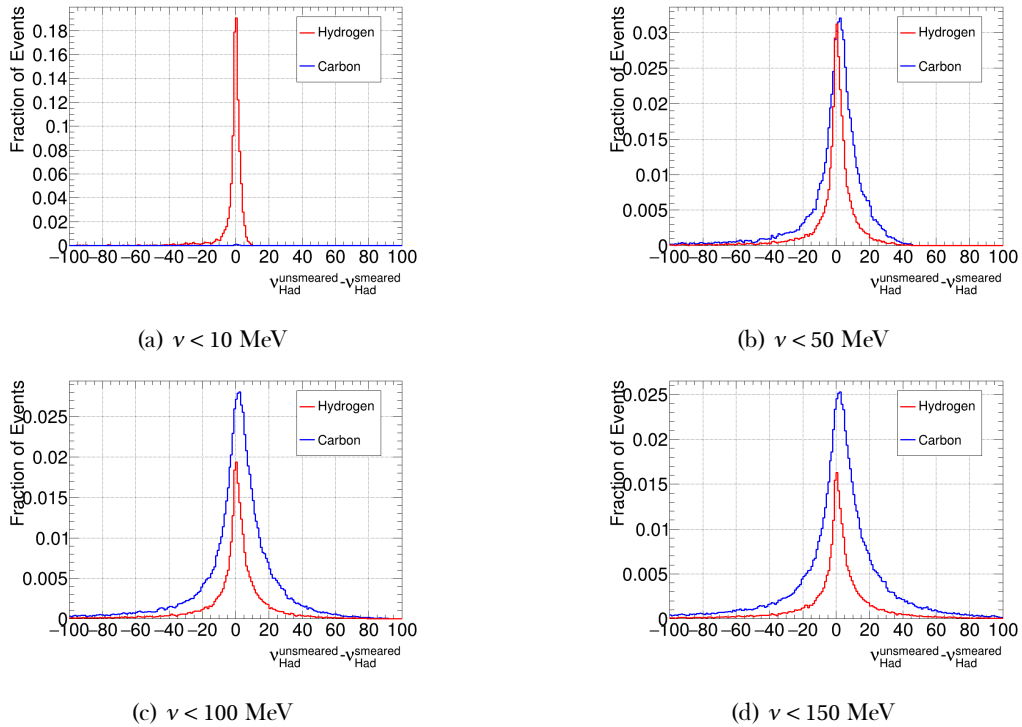(c) $\nu < 100$ MeV

(d) $\nu < 150$ MeV

Figure 15: Effects of neutron smearing at different recoil energies. The effects on hydrogen are smaller than for carbon because they typically have lower energies, which leads to a smaller relative smearing of the time of flight. The carbon contribution is shifted to lower energies due to the higher cross-section for elastic scattering for neutrons coming from carbon. This effect leads to an underestimation of the recoil energy.

III.6 Toy Monte Carlo

To include the detector's effects on the cross-section, the smearing was run 1000 times with different random number seeds for the sampling of the smearing matrix. For each run, the cuts on ν are applied and the cross-section is calculated. In each run, a different number of events will pass a given cut on ν, due to the smearing. When no cut is applied, the cross-sections are identical since the real unsmeared neutrino energy is used for the calculation of the cross-section. The cross-sections for four selected random number seeds and a cut of $\nu < 50$ MeV are depicted in fig. 16. The cross-section distributions for all 1000 random number seeds are shown for four neutrino energy bins in fig. 17. As expected, the effect of the smearing is stronger for the strong cuts on ν compared to the weaker cuts on ν. This is due to the decreasing number of events passing the stronger cuts, leading to larger statistical fluctuations.

(a) $\nu < 10$ MeV   (b) $\nu < 50$ MeV   (c) $\nu < 100$ MeV   (d) $\nu < 150$ MeV
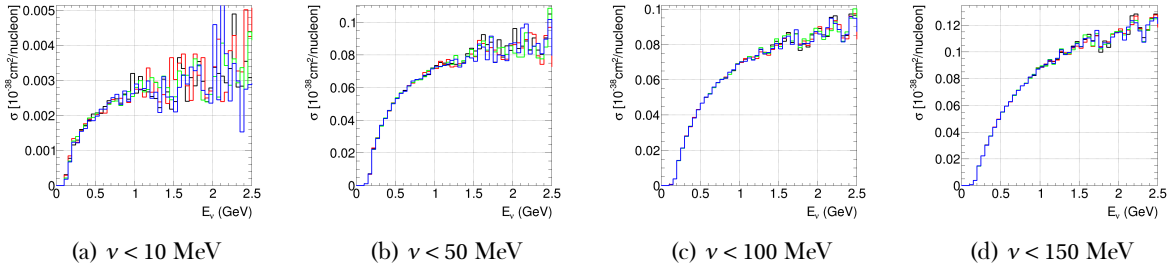
Figure 16: Total cross-section results of four toy Monte Carlo runs with ν cuts. The different colors correspond to different runs of the toy Monte Carlo. For weaker cuts, the different runs are more similar than for stronger cuts.
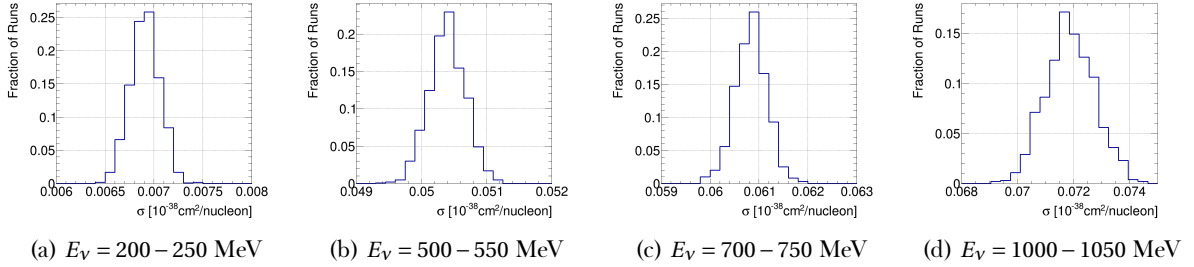

(a) $E_\nu = 200 - 250$ MeV   (b) $E_\nu = 500 - 550$ MeV   (c) $E_\nu = 700 - 750$ MeV   (d) $E_\nu = 1000 - 1050$ MeV

Figure 17: Distribution of the total cross-section for $\nu < 50$ MeV for different neutrino energy bins.

III.7 Evaluation

To finally check for the feasibility of the low-ν method, the flatness of the cross-section has to be evaluated. This is done using a reference point, in this case at 2 GeV. This value of 2 GeV was chosen since the cross-section for the $\nu < 10$ MeV cut becomes constant at this energy. The cross-section histogram is then scaled by $1/\sigma(2GeV)$ to display the fractional cross-section. The result can be seen in fig. 18. In the energy region where the cross-section is constant with respect to 2 GeV, the result would be a straight line at 1. If the fractional cross-section is not equal to 1 above 2 GeV, it means that the cross-section is still increasing and has not reached the region of constant cross-section yet.

Looking at the four different cuts, the mean cross-section for $\nu < 10$ MeV is constant from roughly 2 GeV onwards. This is what is expected from the low-ν method. But at 2 GeV the 1σ interval is given by $[0.78, 1.2]$, and therefore rather large. This is due to the fact, that the detection of these low-energy neutrons is strongly affected by detector effects. Therefore the number of accepted events in this low-ν region strongly fluctuates with each different random number seed. Due to the large standard deviation the cut $\nu < 10$ MeV is challenging to use at T2K neutrino energies.

For weaker cuts the constant part of the cross-section starts at energies above 2 GeV. Since this effect is already seen in the 50 MeV cut, the same problem arises in all the weaker cuts.

Knowledge of the flux in those tail regions still has some value since some information about the flux shape in the peak region can be extracted, but the high statistical fluctuations due to the low number of events in the tail region also make this cut of 50 MeV very challenging in practical applications.

IV   Conclusion & Outlook

In this report the feasibility of the low-ν method for the SuperFGD was discussed. First a perfect detector without any smearing was considered. It was seen that, even in this idealized setup, the low energy peak of the T2K flux makes this method challenging to use due to the low number of neutrino events with a sufficiently high energy. Including the detector smearing shows large statistical uncertainties, especially in the neutrino energy region above 2 GeV where the flux is small.

The used Monte Carlo sample with 1 million events is equivalent to an approximate exposure of 43×10^{21} PoT·ton. The expected number of protons on target for T2K-II is 5×10^{21} PoT [6], which in the case of the 2 ton SuperFGD results in 10×10^{21} PoT·ton. This shows that the used Monte Carlo sample is larger than the statistics expected from the T2K-II run, especially since the expected PoT will be split between neutrino and anti-neutrino beam modes. Therefore the expected statistical fluctuations on the cross-section for T2K-II are larger than the uncertainty mentioned in the previous section. To conclude this analysis, it has to be stated that the low-ν method is very challenging to use at the T2K energies, due to the bad statistics in the region of constant cross-section.

A possible way to extend the low-ν method would be to look at neutrino interactions on hydrogen only since it was shown earlier that the cross-section for these events becomes constant at lower energies compared to neutrino interactions on carbon (see fig. 11). For the tagging of hydrogen events, different methods like kinematic fitting or the $\delta p_\top$ method [5] can be used. A third method which can be used to separate hydrogen from carbon events is to compare E_ν^{CCQE} and $E_\nu^{Cal} = E_\mu + E_{kin,N} + \Delta M$. Here $\Delta M = M_N - M_P$ is the mass difference between the neutron and proton. For hydrogen events and when ignoring detector effects, these should be identical, while they should differ for carbon events. Those two methods could also be combined in future analyses, for example by looking for a region where $\delta p_\top$ is below a certain threshold and where $\left| E_\nu^{CCQE} - E_\nu^{Cal} \right|$ is small. Using only hydrogen events brings with it the problem that only around 1 in 7 protons in the detector are hydrogen, further reducing the number of selected events.
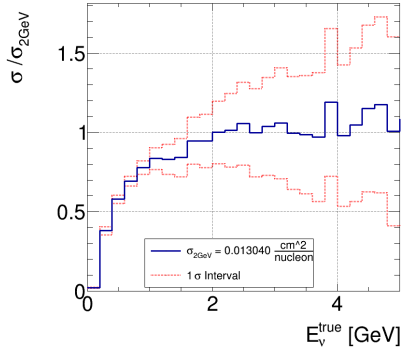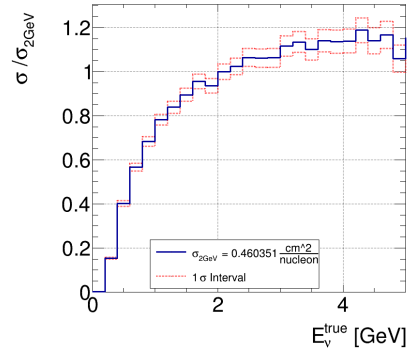
(a) $\nu < 10$ MeV
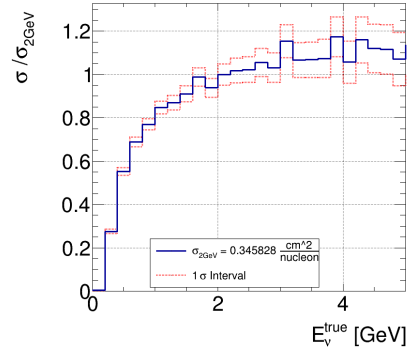
(b) $\nu < 50$ MeV
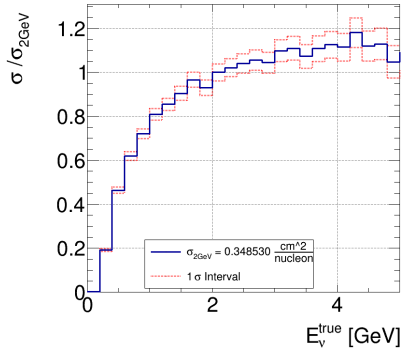
(c) $\nu < 100$ MeV

(d) $\nu < 1/50$ MeV

Figure 18: Fractional cross-section normalized to 2 GeV for different cuts on ν. The blue line shows the mean while the red dotted lines show the standard deviation around the mean, which are obtained from re-running the detector smearing with 1000 different random number seeds. Stronger cuts lead to a bigger standard deviation.

Appendix: Derivation of the low-ν cross-section

This section closely follows [7]. For the derivation of the low-ν cross-section one starts with the general form of the deep inelastic cross-section:

$$\frac{\mathrm{d}^2\sigma}{\mathrm{d}x\mathrm{d}y} = \frac{G_F^2 y}{16\pi} \frac{1}{\left(1 + \frac{q^2}{M_W^2}\right)^2} L^{\mu\nu} W_{\mu\nu} \tag{13}$$

Here it is assumed that it is possible to develop the hadronic tensor in structure functions $W_i(x, q^2)$. With this, the leptonic and hadronic tensors are given by:

$$L^{\mu\nu} = 2Tr\left((\not{k}' + m)\gamma^\mu(1 - \gamma^5)\not{k}\gamma^\nu\right) \tag{14}$$

$$W^{\mu\nu} = -\eta^{\mu\nu} W_1 + \frac{p^\mu p^\nu}{M^2} W_2 - i\epsilon^{\mu\nu\lambda\sigma} \frac{p_\lambda q_\sigma}{2M^2} W_3 + \frac{q^\mu q^\nu}{M^2} W_4 + (p^\mu q^\nu + p^\nu q^\mu) W_5. \tag{15}$$

Using the trace theorems and assuming that the lepton mass is negligible one finds:

$$L^{\mu\nu} = 4\left(k'^\mu k^\nu - k' \cdot k\, \eta^{\mu\nu} + k'^\nu k^\mu - i\epsilon^{\beta\nu\alpha\mu} k'_\alpha k_\beta\right). \tag{16}$$

For the hadronic tensor, changing to dimensionless structure functions $F_i(x, q^2)$ using a scaling with M/ν for $i = 2, 3, 4$ is the next step. Further assuming that the exchanged momentum q^2 is smaller than M_W^2 results in the dropping of the last two terms proportional to W_4 and W_5. Now one has:

$$W^{\mu\nu} = -\eta^{\mu\nu} F_1 + \frac{p^\mu p^\nu}{M^2 \nu} F_2 - i\epsilon^{\mu\nu\lambda\sigma} \frac{p_\lambda q_\sigma}{2M^2 \nu} F_3. \tag{17}$$

Introducing the standard parameters:

$$\nu = \frac{p \cdot q}{M}, \qquad x = \frac{q^2}{2M\nu}, \qquad y = \frac{p \cdot q}{p \cdot k} \tag{18}$$

one can rewrite, again under the assumption that the lepton mass is zero the double differential cross-section as:

$$\frac{\mathrm{d}^2\sigma}{\mathrm{d}x\mathrm{d}y} = \frac{G_F^2 M E_\nu}{\pi} \left[\left(1 - y - \frac{Mxy}{2E_\nu}\right) F_2 + \frac{y^2}{2} 2xF_2 \pm y\left(1 - \frac{y}{2}\right) xF_3\right]. \tag{19}$$

Introducing the parameter $R_L = F_2/2xF_1$, substituting $y = \nu/E$, $Q^2 = 2M\nu x$ and grouping the terms by powers of ν/E, one finally finds the wanted cross-section:

$$\frac{\mathrm{d}\sigma}{\mathrm{d}\nu} = \frac{G_F^2 M_\mathcal{N}}{\pi} \int_0^1 \left(F_2 - \frac{\nu}{E_\nu}[F_2 \mp xF_3] + \frac{\nu}{2E_\nu^2}\left[\frac{M_\mathcal{N} x(1 - R_L)}{1 + R_L} F_2\right] + \frac{\nu^2}{2E_\nu^2}\left[\frac{F_2}{1 + R_L} \mp xF_3\right]\right)\mathrm{d}x \tag{20}$$

REFERENCES

[1] J. Devan et al, *Measurement of the inclusive Neutrino and Antineutrino charged current cross sections in MINERvA using the low-ν flux method*, Physical Review D 94, 2016

[2] T. Kikawa, *Measurement of Neutrino Interactions and Three Flavour Neutrino Oscillations in the T2K Experiment*, Springer, 2016

[3] D. Sgalaberna, Neutrino Physics - Lecture at ETH Zürich in HS 2020

[4] Y. Hayato, *A Neutrino Interaction Simulation Program Library NEUT*, Acta Physica Polonica B, 2009

[5] L. Munteanu et al. *New method for an improved antineutrino energy reconstruction with charged-current interactions in next-generation detectors*, Physical Review D 101, 2020

[6] T2K Collaboration, ND280 Group, *T2K ND280 Upgrade, Technical Design Report*, arXiv:1901.03750v2

[7] J. Devan, *Measurement of Neutrino and Antineutrino Charged-Current Inclusive Cross Section with the MINERvA Detector*, PhD Thesis, College of William and Marry, 2016